Online Supplement:

Experimental Methods and Results

Detailed Methods

Ethical Approval

All experiments were approved by the University Committee on the Use and Care of Animals (UCUCA) at the University of Michigan, and the Department of Laboratory Animal Resources and the Committee for the Humane Use of Animals (DLAR-CHUA) of SUNY Upstate Medical University. All euthanasia was performed following the recommendations of UCUCA and DLAR-CHUA. All mother rats were either donated to the university "rat recycling program" for use by other investigators, or euthanized by placing the rat in a carbon dioxide filled chamber, followed by removal of a vital organ (e.g., heart). The neonatal rats were euthanized by quick decapitation.

Cultured Neonatal Rat Ventricular Myocytes:

Neonatal rat ventricular myocytes (NRVM) were obtained from 1-2 day old Sprague Dawley rat (Charles River) hearts.(Rohr *et al.*, 2003) The hearts were excised and the lower $^{2}/_{3}^{rds}$ of the ventricles were collected and minced in Hank's balanced salt solution (HBSS) without calcium and magnesium (Cellgro). The ventricular tissue was enzymatically digested through serial incubation steps in 0.064% trypsin (Roche Applied Sciences), and 85 µg/mL pancreatin (Sigma). The supernatant from each step was added to a solution containing Media M199 (Cambrex) supplemented with 10% fetal bovine serum (FBS, Cellgro). The cells were later centrifuged (800 RPM), resuspended

in fresh M199 and 10% FBS, and the cells were pre-plated for 2 hours to minimize the nonmyocyte population. The myocytes ($1.2x10^6$ cells) were plated on 25mm glass collagen coated (human placental collagen Type-IV, Sigma) coverslips (Fisher Scientific) in 35mm wells or cell culture treated 35mm plastic dishes (Corning), and maintained in M199 supplemented with 10% horse serum (Invitrogen), bromodeoxyuridine (30 uL/ml, Sigma), and 20 units/mL of penicillin and 20ug/mL streptomycin. Media was changed 24 and 48 hours after plating with the above mentioned 10% horse serum enriched media. The myocyte monolayers were stored in an incubator (37^oC, 5% CO_2, VWR) and all experiments were performed after 4-5 days in culture.

Photolithographic Patterning:

We used a technique derived from that originally published by Rohr et al(Rohr *et al.*, 2003). Glass coverslips were cleaned and then spin coated with KTFR Photoresist (Alphametals, USA.). The photoresist coated coverslips were baked for 2 hours at 80^oC, and exposed to UV light while in close contact with a film mask carrying the desired pattern. UV light stabilized the photoresist, and immersion in xylol washed away the photoresist coating from the areas of the coverslip that were not exposed to the UV light (areas where cell attachment was desired). On the day of the myocyte dissociation the coverslips were coated with collagen and left in distilled water at 37^oC for 1 hour. This softened the photoresist and facilitated it to be pealed off of the glass coverslip. Removal of the photoresist resulted in collagen only present in the desired myocyte monolayer pattern. As shown in Figures 1A and 2A, this technique was utilized

to create the two expansion regions (6mm long x 9mm wide), connected by a thin isthmus (6mm long, and precise widths ranging from 0.1 – 2 mm wide).

Adenoviral Transfer

The laboratory of Dr. Silvia Priori (IRCCS Fondazione Maugeri, Pavia, Italy) graciously provided a viral construct containing the wild-type human SCN5a sequence (Ad-Nav1.5). Adenovirus encoding green fluorescent protein (GFP) was obtained from Dr. Steven Taffet (SUNY Upstate Medical University, Syracuse, New York). For each construct the sequence was inserted into the shuttle vector (pShuttle1.1). The cDNA was subcloned into the pAd/CMV/V5-DEST adenoviral expression system (Clontech).

Recombinant adenoviruses encoding hSCN5a and GFP were generated using the Adeno-X Expression System (Clontech). Purified (Virus Purification Kit, Clontech) and titered (Rapid Titer Kit, Clontech) virus was applied to myocyte monolayers at various levels of multiplicity of infection. After 2 days in culture, myocytes were infected with the Ad-Nav1.5 or Ad-GFP (viral control) virus and incubated for 48-72 hours, resulting in a significant increase in hNav1.5 or GFP protein expression.

The optimal viral concentration was determined through a multipart systematic approach to assure: (1) cell viability (phase microscopy, OLS Figure 1A), (2) efficient (Western blot, Figure 3A and OLS Figure 1D) and homogeneous (immunolocalization, OLS Figure 1C) viral infection and expression, (3) increased I_{Na} (Figure 3B-D), and (4) uniform change in the velocity of impulse propagation and APD in monolayer preparations (Figures 3E & 5C). A multiplicity of infection (MOI) of 10 was found to be optimal for the Ad-Nav1.5 and Ad-GFP constructs based upon these tests. No

differences in cell appearance, uniform spread of the electrical impulse, CV (Figure 3E), or APD (Figure 5C) were observed between Ad-GFP expressing and uninfected monolayers.

DNA Sequencing of the Coding Region of the Viral Construct

The Ad-Nav1.5 adenoviral construct was sequenced around the gene insert. The entire 6.05kB was inserted with 99.9% sequence identity to 9 complete human cDNA sequences available on the NCBI website (greatest similarity to AY148488.) There was a single previously undocumented nucleotide difference in the adenoviral construct (G→A) resulting in an amino acid change at site 558 of a threonine to alanine. Based upon consultation with Dr. Karen L. Vikstrom and Dr. Miriam Meisler's laboratory at the University of Michigan (expert molecular biologist and geneticist in the field) and genome searches, it was predicted that this amino acid change would not have any functional effects. They are both weak amino acids, likely yielding a conservative/inert amino acid change within the DI-II intracellular linker domain. The amino acid at site 558 is not evolutionarily conserved and quite variable between species; an alanine at site 558 is present in the opossum and small hedgehog. The genetic sequencing data along with the protein blotting, immunolocalization, and voltage-clamp data confirmed that infection with the hSCN5a construct yielded hNav1.5 protein expression, and functional wild-type I_{Na} (Figures 3 & 4, & OLS Figure 2 & 3).

Single Cell Electrophysiology

Experiments were carried out using a Multiclamp 700B amplifier (Axon Instruments, Union City, CA). The data were acquired and analyzed using the pCLAMP 10 Suite of programs (Axon Instruments, Union City, CA). Borosilicate glass electrodes were pulled with a Brown-Flaming puller (model P-97), yielding appropriate tip resistances when filled with pipette solution to enable proper voltage/current control.

Current Clamp:

Whole cell current-clamp AP experiments were performed, in which the stimulus pulse (5ms duration) was generated using a stimulator (World Precision Instruments DS8000.) The myocytes were paced at 0.5Hz and from 1 Hz up until loss of 1:1 capture of stimulus to AP response, in 1 Hz increments. The cells were superfused with HBSS w/ Ca^{2+} and Mg^{2+} (Sigma.) The intracellular solution consisted of 1mM $MgCl_2$, 5mM EGTA, 150mM KCl, 5mM HEPES, 5mM Phosphocreatine, 4.5mM K_2ATP, 2mM B-Hydroxybutyric acid. Recordings were performed at 37° C.

Voltage Clamp:

Whole cell voltage-clamp was used to measure I_{Na}. To ensure adequate voltage control, experiments were performed at room temperature (21-22°C) with pipette resistances $\leq$3 MΩ when filled with the pipette filling solution and 20mM $[NaCl]_o$. The extracellular solution contained: 20mM NaCl, 1 mM $MgCl_2$, 1.8mM $CaCl_2$, 0.1mM $CdCl_2$, 11mM Glucose, 117.5mM CsCl, and 20mM HEPES, pH 7.35 with CsOH. The filling

solution contained: 5mM NaCl, 135mM CsF, 10mM EGTA, 5mM MgATP, and 5mM HEPES, pH 7.2. Appropriate whole-cell capacitance and series resistance compensation (≥70%) was applied, along with leak subtraction. In order to assess the I_{Na} density, the cells were held at -120 mV and stepped to various test potentials (-80 to 30 mV, 5mV increments, 200 ms duration, 2800ms interpulse intervals). Steady-state sodium channel availability was determined by holding at various potentials (-160mV to -25mV, 5mV increments, 300ms duration) and stepping to -30mV (20ms), with 2680ms interpulse intervals. The voltage dependence of I_{Na} activation and availability curves were fitted using a Boltzmann function. Time-dependent recovery was determined by holding at -120mV and stepping to -30mV (P1) for 20ms, then returning to -120mV for 2-80ms (2ms increments) and stepping again to -30mV (P2) for 20ms. The time-dependent recovery was P2/P1 at each time point and was fitted using a single exponential function.

Western Blot

We collected whole cell protein lysates and probed for Nav1.5 in four separate instances 48 hours after viral infection. The NRVMs were collected in cold Tris-EGTA (pH 8) with Complete Protease Inhibitor cocktail (Roche). The cells were pelleted (5000 RPM, 5 minutes) and resuspended in RIPA lysis buffer containing protease inhibitor, and incubated on ice for 30 minutes. Following a second centrifugation (13000 RPM, 10 minutes) the supernatant was retained to remove the cellular debris. Next, 10 µL of 6XSSB was added to each 50 µL sample and run on a 4-12% tris-glycine gel (Invitrogen) in Running Buffer (Fisher). The protein was transferred onto a 0.45µm

nitrocellulose membrane overnight in Transfer Buffer (Fisher) with 20% methanol. The membrane was later blocked for 24 hours at 4^{o}C in 5% nonfat dry milk with tris buffer saline with 0.1% Tween20, and incubated with the primary antibody (rabbit Nav1.5, Upstate, or mouse monoclonal GAPDH, RDI) and secondary antibody (anti-rabbit or anti-mouse HRP, Sigma, respectively) for 1 hour. The signal was detected using Chemiluminescence (Pierce).

Optical Mapping of Electrical Impulse Propagation

The monolayer was positioned in a continuous flow (7mL/min), homogeneous temperature controlled apparatus (37±0.5^{o}C, Cell MicroControls), and superfused with HBSS with Ca^{2+} and Mg^{2+} (Sigma). The preparations were stained with a potentiometric dye (40 μM di-8-ANEPPS, Molecular Probes). High-resolution recordings were acquired using 360 watt halogen lamps, infrared (heat), 535nm (green), and 645nm (red) filters, and an 80x80 pixel CCD camera (285μm or 438μm per pixel, and 200 frames per second, SciMeasure Analytical Systems Inc.) The optical signals were amplified, filtered, digitized (Lab-Windows acquisition), and stored on a Dell P4 personal computer.(Munoz *et al.*, 2007) Analytical tools to examine impulse propagation were developed by members of the laboratory(Gray *et al.*, 1995). The optical recordings/movies undergo a standard set of digital processing, including both spatial and temporal filtration. The average APs are from each of the horizontal rows of pixels across the preparation (2mm wide isthmus divided by 0.285 mm/pixel = average of 7 horizontal lines through the preparation). Further details on the filtration procedures and how they impact upon the signal to noise ratio and true signal can be found in Mironov

et al. (2006)(Mironov *et al.*, 2006). At each frequency we acquired 3 movies (5 seconds each). Pacing was continuous during the initial 2 movies, and midway through the 3rd movie pacing was ceased to potentially facilitate a reflected wave to retrogradely propagate back through the entire preparation without colliding with a subsequent paced wave.

Criteria for Inclusion of Preparation:

We set the following six criteria for the inclusion of monolayers: (1) The cells must appear viable and confluent under phase microscopy (OLS Figure 1A). (2) There must be homogeneous viral expression across the monolayer, as assessed by immunoflurescent staining (OLS Figure 1C). (3) There cannot be any unexcitable regions within the NRVM monolayer. (4) There must be the uniform spread of the electrical impulse in homogeneous preparations. (5) There cannot be conduction block at the proximal entrance to the isthmus (rarely seen, 4 of 140 preparations). (6) As EADs and reflection are known to occur at low excitation frequencies, the preparation must visit at least one of the excitation frequencies between 1–5Hz during the course of the experiment. For all analysis we were blinded to which group each recording belonged.

Pharmacological Challenges

The following pharmacological agents were used to: 1) block the sodium current, 30 μM tetrotoxin (TTX, Sigma); 2) increase the persistent I_{Na}, 0.01–30μM veratridine (Sigma); 3) I_{CaL} agonist, 1 μM Bay K 8644 (CalBiochem). We alternated the

order of solution delivery with each preparation to rule out potential run down or deterioration of a dish affecting the possibility of reflection.

Results

Biophysical Properties of Endogenous and Virally Expressed I_{Na}

To assess the ionic mechanism(s) underlying the promotion of reflection by the increased I_{Na} we performed single cell voltage and current-clamp AP recordings to examine the biophysical properties of I_{Na} and their implications upon the AP morphology and duration.

The effects of Ad-Nav1.5 expression (Figure 3A), and thus increased I_{Na} density (Figure 3B-D) were observed in single-cell current-clamp AP recordings. Ad-Nav1.5 expression led to a significant increase in the AP upstroke velocity at the four pacing cycle lengths tested (OLS Figure 2A). The AP upstroke velocity increased from 114.2±10.2mV/ms (uninfected) and 121.1±11.5mV/ms (Ad-GFP) to 215.3±6.9mV/ms (Ad-Nav1.5) at a pacing cycle length of 1000 ms ($p<0.05$).

The biophysical properties of the endogenous (Uninfected and Ad-GFP) and virally expressed (Ad-Nav1.5) I_{Na} were very similar. Their normalized current-voltage relationships overlapped (OLS Figure 2B) and the voltage of peak inward current was similar in all groups (OLS Figure 2C). The voltage dependence of I_{Na} activation (m-infinity curve) was fitted using a Boltzmann function. The $V_{1/2}$ of I_{Na} activation (-48.32±1.93mV for uninfected, -47.87±1.83mV for Ad-GFP, and-51.53±1.66mV for Ad-Nav1.5) and slope factors (4.33±0.31 for uninfected, 4.84±0.36 for Ad-GFP, and

4.18±0.27 for Ad-Nav1.5, OLS Figure 2D) were similar in each of the three groups (p=ns).

The voltage dependence of I_{Na} availability (h-infinity curve) was fitted using a Boltzmann function (OLS Figure 2D). The slope factors did not differ between groups (6.69±0.33 for uninfected; 6.56±0.30 for Ad-GFP; and 6.12±0.50 for Ad-Nav1.5.) The Ad-Nav1.5 $V_{1/2}$ of I_{Na} availability (-97.01±2.46mV) was left-shifted compared to uninfected (-85.29±3.53mV, $p<0.05$) and Ad-GFP (-91.55±6.58mV, p=ns). This difference was in agreement with the work of Stocker et al. 2006(Stocker & Bennett, 2006), in which the $V_{1/2}$ of I_{Na} availability was left-shifted for adult (virally expressing I_{Na}), compared to neonatal myocytes (endogenous I_{Na} in the Uninfected and Ad-GFP groups).

The time dependence of I_{Na} recovery from inactivation (0-80ms, 2ms intervals) was fitted with a single exponential function. All three fits overlapped and were virtually identical, without any significant differences in the time constants (7.23±1.86 for Uninfected; 9.90±1.88 for Ad-GFP; and 8.24±1.50 for Ad-Nav1.5, OLS Figure 2E.)

The fast component of I_{Na} inactivation was significantly faster in the Ad-Nav1.5 group; albeit, there was a trend for the slow component to be slower at the voltages of maximal I_{Na} (significant at -30mV, OLS Figure 3).

Computer Simulations

Detailed Methods

Cable

We simulated a 1D cable of 8800 nodes, with each node corresponding to Δx=0.1mm. Internodal conductance was 0.00024mS with embedded synthetic curvature (see below). Cells were modeled using LR2000 model(Faber & Rudy, 2000), with calcium release triggered by voltage crossing -35 mV and a customized model of sodium current.

The one-dimensional (1D) cable was simulated using the following differential equation:

$$\frac{\partial V_m}{\partial t} = D \cdot \frac{\partial^2 V_m}{\partial x^2} + D \cdot \kappa \cdot \frac{\partial V_m}{\partial x} + i_{stim} - i_{ion}, \quad \text{(Eq. 1)}$$

When $\kappa(x) = 0$ (i.e. curvature is assumed zero throughout the entire cable), (Eq. 1) is reduced to a classic 1D cable equation of impulse propagation. On the other hand, for a hyperbolic decay, in which $\kappa(x) = \frac{1}{x}$, then (Eq. 1) describes impulse propagation in a polar coordinate system. We performed computer simulations in a 1D cable using several assumptions on $\kappa(x)$.

(Eq. 1) was discretized using Finite Difference Method (FDM):

$$\begin{cases} g_{[n+1\to n]} = g_0(1+\kappa\Delta x) \\ g_{[n-1\to n]} = g_0(1-\kappa\Delta x) \end{cases}, \quad \text{(Eq. 2)}$$

where $g_{[n+1\to n]}$ is the internodal conductance used to calculate current flow into node n from node $n+1$, $g_{[n-1\to n]}$ is internodal conductance used to calculate current flow into

node n from node $n-1$, and Δx is the spatial resolution of the FDM grid. g_0 is a nominal internodal conductance satisfying equation

$$\frac{g_0}{C_0} = D \cdot \frac{1}{\Delta x^2}, \qquad \text{(Eq. 3)}$$

where $C_0 = 153.4\,\mathrm{pF}$ is cell capacitance attached to every node of the FDM grid.

Accordingly, electrotonic current received by a computational cell was

$$i_{e[n]} = g_{[n-1\to n]}\left(V_{m[n-1]} - V_{m[n]}\right) + g_{[n+1\to n]}\left(V_{m[n+1]} - V_{m[n]}\right), \qquad \text{(Eq.4)}$$

where $i_{e[n]}$ is the electrotonic current being received by the n-th computational cell (node), $V_{m[n]}$ is the transmembrane voltage in the n-th computational cell.

To effectively search the parameter space for persistent I_{Na}, we simulated a 1D cable of 8800 nodes in length, with each node corresponding to 0.1mm. Internodal conductance was 0.00024 mS. The cable was composed of 11 segments of 800 nodes each, and for each segment we assumed a specfic value of curvature κ, which was constant within every segment.

Virtual curvature was introduced in the following way: In a classic simple 1D cable, the equation describing transmembrane voltage can be written as:

$$\frac{\partial V_m}{\partial t} = \frac{\sigma_{2D}}{\beta_{2D} C_m} \cdot \frac{\partial^2 V_m}{\partial x^2} + i_{stim} - i_{ion},$$

where V_m is the transmembrane voltage, t is time, σ_{2D} is the 2D specific conductance, β_{2D} is a 2D surface-to-"volume" ratio, C_m is the membrane specific capacitance, x is a geometrical coordinate along the cable, and i_{stim}, i_{ion} are, respectively, the stimulation

and ionic currents (normalized to cell capacitance). Discretization of the spatial derivative using Finite Difference method leads to the well known equation for the electrotonic current being received by a cell:

$$i_{e[n]} = g_{[n-1\leftrightarrow n]}\left(V_{m[n-1]} - V_{m[n]}\right) + g_{[n\leftrightarrow n+1]}\left(V_{m[n+1]} - V_{m[n]}\right),$$

where $i_{e[n]}$ is the electrotonic current being received by the n-th computational cell (node), $V_{m[n]}$ is the transmembrane voltage in the n-th computational cell and $g_{[n\rightarrow n+1]} = g_{[n+1\leftarrow n]}$ is a conductance between the n-th and $n+1$-th node. In the case of a homogeneous cable, we can use one constant $g_{2D} = g_{[n\rightarrow n+1]} = g_{[n+1\leftarrow n]} = \sigma \cdot \Delta x$ for the entire cable and

$$g_{2D} = \sigma_{2D} \cdot \frac{\Delta x}{\Delta x}$$

$$C_0 = C_m \cdot \beta_{2D} \Delta x^2$$

$$\frac{g_{2D}}{C_0} = \frac{\sigma_{2D}}{C_m \cdot \beta_{2D} \Delta x^2} = \frac{\sigma_{2D}}{C_m \cdot \beta_{2D}} \cdot \frac{1}{\Delta x^2}$$

However, in the case of a 2D concentric wavefront, because of circular symmetry, the following applies:

$$\frac{\partial V_m}{\partial t} = \frac{\sigma_{2D}}{\beta_{2D} C_m} \cdot \frac{\partial^2 V_m}{\partial r^2} + \frac{\sigma_{2D}}{\beta_{2D} C_m} \cdot \kappa \cdot \frac{\partial V_m}{\partial r} + i_{stim} - i_{ion}$$

where r is the distance from the center and $\kappa = \frac{1}{r}$ is the local curvature at distance r. This allowed us to model curvature in a 1D cable, using a Finite Difference Method:

$$\begin{cases} g_{[n+1\to n]} = g_{2D}(1+\kappa\Delta x) \\ g_{[n-1\to n]} = g_{2D}(1-\kappa\Delta x) \end{cases}.$$

Importantly, for any non-zero curvature, the symmetry is now lost ($g_{[n\to n+1]} \neq g_{[n+1\leftarrow n]}$).

The 1D simulations were used to overcome several limitations existent in 2-dimensions. First, the 1-dimensional cable enabled us to examine many curvatures within the same simulation for each persistent to peak I_{Na} condition, which facilitated us to precisely determine the combination of curvature, persistent I_{Na}, and peak I_{Na} needed for EAD formation and reflection. Second, the 1-dimensional cable enabled us to rule out the influence of boundary conditions, and see what effect an abrupt expansion (increased curvature) had upon reflection. Finally, our 1-dimensional approach allowed us to clearly rule out micro-reentry. Each segment of the cable simulated a constantly increasing wavefront curvature. Previous studies (Kucera *et al.*, 1998;Rohr & Kucera, 1997;Rohr *et al.*, 1999;Rohr & Salzberg, 1994;Cabo *et al.*, 1994) have extensively implicated the effects of abrupt geometrical expansions upon wavefront curvature, source-to-sink relations, and the stability of impulse propagation. These simulated expansions served to reproducibly model these same effects (OLS Figure 5B-C), and enable us to establish a model to precisely dissect out the mechansisms for APD prolongation, EAD formation, and reflection.

Sodium current

Fast sodium current was modeled as

$$i_{Na} = G_{Na} \cdot m^3 h \cdot (V_m - E_{Na}),$$

where G_{Na} is the sodium current conductance, m and h are the gating variable and E_{Na} is the reversal potential for sodium. The rationale was to simplify the model, as the specific molecular mechanisms for the persistent I_{Na} and the time-dependent recovery of the current were beyond the scope of the study. The model enabled us to easily control the level of persistent I_{Na} using one parameter (h_{floor}).

Gating variables in the steady state were modeled as

$$m_{\infty} = m_{floor} + \left(1 - m_{floor}\right) \cdot \frac{1}{1 + \exp\left(\frac{V_m - V_{half(m)}}{k_{(m)}}\right)}$$

$$h_{\infty} = h_{floor} + \left(1 - h_{floor}\right) \cdot \frac{1}{1 + \exp\left(\frac{V_m - V_{half(h)}}{k_{(h)}}\right)}$$

with fixed time constants $\tau_m = 0.05\,\text{ms}$ and $\tau_h = 2.5\,\text{ms}$. We assumed $V_{half(h)} = -86.1\,\text{mV}$, $k_{(h)} = 8.17\,\text{mV}$, $V_{half(m)} = -61.4\,\text{mV}$, $k_{(m)} = -6.44\,\text{mV}$, $m_{floor} = 0.021$ based on a best fit to the patch-clamp data. Values of G_{Na} and h_{floor} (surrogate for persistent I_{Na}) were changed from simulation to simulation to investigate their effect on the incidence of reflection.

Numerical Results

Simulated I_{Na}

In OLS Figure 4A are the I_{Na} traces from a simulated voltage-clamp experiment using a model of fast sodium current, with E_{Na}=36mV, to match our *in vitro* experimental

data (Figure 3B). OLS Figure 4B shows an I-V relationship obtained from the traces. The model reproduced the I-V relationship obtained experimentally (Figure 3C). Similar to the *in vitro* result, the voltage of peak inward current was -40mV (OLS Figure 4B).

Virtual Curvature

Electrical waves propagating through areas of tissue expansion experience significant slowing as a result of source-to-sink mismatch related to increased wavefront curvature (Figure 1).(Cabo *et al.*, 1994;Rohr *et al.*, 1999) However, whether curvature and source-to-sink mismatch also affect the APD has not been investigated. Therefore, we conducted numerical simulations to test whether a change in local curvature simulating a structural heterogeneity, in combination with an increase in persistent I_{Na}, would result in APD prolongation, EADs and reflection. As presented in detail in OLS Figures 5-7, we simulated a cable of 8800 nodes (1 node=0.1mm). The curvature $\kappa(x)$ varied along the cable, as shown in OLS Figure 5A, so that the cable was composed of 11 segments. For each segment we assumed a specfic value of curvature κ, which was constant within every segment: from 0 (planar wavefront) in the first segment to 0.050 node^{-1} (0.50 mm^{-1}, highest curvature) in the last segment. A simulation using this 1D cable, with h_{floor}=0.005 and G_{Na}=1.76mS/µF is shown in the TSP of OLS Figure 5B. A single wave initiated at the left end propagated through the entire cable with a gradual reduction in CV as the local curvature increased, illustrated by the wavefront diverging from the straight red line marking the initial CV. Most important, the APD depended on the local curvature, with the shortest APD in the planar segment and the longest APD in the segment with largest curvature (OLS Figure 5C).

OLS Figure 5D shows a simulated AP traveling through a cable with slightly higher I_{Na} density (G_{Na}=1.80mS/µF). As OLS Figure 5E illustrates, the AP prolonged with increasing curvature. At 640mm, the curvature increased from 0.035 to 0.040 node^{-1}, i.e from 0.35 to 0.40 mm^{-1}. At the expansion (red trace) a subthreshold EAD is seen, followed by a brief repolarizarion. The AP at the first site of re-excitation (641.3mm, light blue trace) did not fully repolarize, with re-excitation arising during phase-3 of the AP, similar to that seen at the distal expansion in Figure 7D. The neighboring proximal, 640mm (red), fully repolarizes and then is re-activated by the retrograde propagating reflected response. The downstream site, 680mm (purple) is too later re-activated by the second propagated response, which originated from the distal expansion region (i.e. 641.3mm). Please note that the APs preceding the reflected response are aligned so the upstrokes all occur at t=0. Importantly, using these model kinetics we did not observe single cell EADs, or re-excitation and reflection when impulses propagated towards regions of smaller and smaller curvature, or 1D cables without changing curvature. As shown in OLS Figure 5F, an additional increase in I_{Na} (G_{Na}=1.84mS/µF) also generated an EAD and reflection, in this case at 1.8mm from the pacing site, even without the necessity of a structural substrate (zero local curvature).

In OLS Figure 6, we show measurements of parameters recorded close to the reflection site (denoted by the red vertical lines in OLS Figure 5D). In OLS Figure 6A-C the APs preceding the reflected response are aligned so the upstrokes all occur t=0. In panel B, the location in time of the late I_{Na} is progressively delayed/prolonged with increasing curvature. In panel C, a similar delay/prolongation occurs for I_{CaL}; at 641.3 mm there is slow reactivation of I_{CaL}, which coincides with the reflected AP.

To gain better insight into the role of structure and wavefront curvature, we obtained recordings at each of the 60 nodes (6.0 mm) surrounding the site of re-excitation (630 mm ≤ x ≤ 643 mm) and displayed them in an analogous way as in the experiment of Figure 2B; the first black recording at 640mm denotes the site of the step increase in curvature. In the presence of 0.35mm^{-1} curvature, prior to the step increase in curvature (x < 640mm) there was a small "hump" at the end of the AP (OLS Figure 6D). As the anterograde AP entered the region of higher curvature (640mm, black APs), the "hump" occurred later during phase-3, along with increased depolarizing electrotonic current being received by the cells. In OLS Figure 6E, we present the electrotonic current being received by the cells located in the vicinitiy of the site of re-excitation, proportional to $\frac{d^2V_m}{dx^2}$. Two features in that graph are obvious: large, biphasic spikes around 6200 ms (corresponding to anterograde propagation) and around 6600 ms (corresponding to the reflected wave). As shown in Panel E, one can find a tiny hump between 6450 and 6550 ms. This electrotonic hump mediates the reflection. First, the height and timing of that hump results from the AP shape ($\frac{d^2V_m}{dx^2}$), which then depolarizes the membrane potential to the threshold for re-excitation. In panel E2, at x < 641.3 mm the rising slope of the hump of the antegrade electrical wave is clearly distinguishible from the rising slope of retorgrade propagation; however at x=641.3 mm the two become fused, illustrating the site of re-excitation. All of this is consistent with the relationship between APD and curvature, presented in OLS Figure 5C.

Source-to-Sink Mismatch Increases the APD

We measured the APD_{80} at each node leading up to and through the re-excitation and reflection site at 641.3mm, which was just downstream of the step increase in curvature from 0.035 to 0.040 $node^{-1}$, i.e. from 0.35 to 0.40 mm^{-1} at 640 mm at 640mm. We used the model kinetics that did (G_{Na} 1.80mS/µF, OLS Figure 5D) and didn't (G_{Na}=1.76mS/µF, OLS Figure 5B) produce reflection at this site. There was progressive APD_{80} prolongation with increasing curvature. Using the model kinetics that didn't produce reflection, the APD_{80} increased from 230ms at 0mm (no curvature) to 256ms at 560mm (data not shown). In the presence of increased G_{Na} (1.80mS/µF) the effect was even larger, as it increased from 234ms (0mm) to 272ms (560mm), which was upstream from the site of re-excitation. This information demonstrated that the combination of structure and increased persistent I_{Na} was sufficient to facilitate APD prolongation, even before being able to fire a full EAD. Using the model kinetics with G_{Na}=1.80mS/µF, and even larger curvature (~641.3mm), the conditions were sufficient to produce re-excitation and reflection (OLS Figure 5E).

Using the same G_{Na} used in OLS Figure 5B, D, & F, stimulation was applied to the right hand side of the cable. As the impulse propagated towards regions of smaller and smaller curvature the APD remained the same (<5% change in the APD). In addition, a simple 1D cable without changing curvature also showed no change in the APD. Finally, in all of these simulations in which propagation went from a region of large to small curvature, reflection was never observed.

To address the relationship between curvature (structure) and I_{Na} density (both peak and persistent), we performed a set of simulations similar to those shown in OLS

Figure 5B, D and F, using a wider range of values for G_{Na} and h_{floor} to determine the curvature necessary for reflection. We tested four values of h_{floor} (0.0050, 0.0075, 0.0100 and 0.0150), which yielded I_{Na} persistent-to-peak current ratios of 0.98%, 1.27%, 1.55% and 2.13%, respectively, and covered the range of persistent current level seen experimentally in Figure 4C. The results are summarized in OLS Figure 7. In Panel A, when I_{Na} conductance increased (arrows 1→2), the level of curvature necessary for reflection decreased sharply for all tested levels of persistent current. The parameter space of the peak and persistent I_{Na} (panel B) illustrated the range of parameters within which an EAD/reflection may or may not occur in the absence of a structural substrate (increased curvature). In Panel B, there is a line denoting the necessary peak and persistent I_{Na} for reflection of a planar wavefront. All values below this line require the additional contribution of a geometrical expansion to facilitate reflection as the persistent I_{Na} density was too low to facilitate an EAD mediated reflected response.

Therefore, the change in the source-to-sink relations due to the structure, prolonged/delayed/reactivation of I_{Na} and I_{CaL}, and the increased depolarizing electrotonic current being received by the cells all provided a mechanism for APD prolongation and EAD formation at geometrical expansions.

Limitations

In the simulation with virtual, segment-specific curvature, we used an extremely, unphysiologically, long cable. In addition to providing us with the ability to effectively search parameter space for I_{Na}, this type of simulations provided us with a unique opportunity. For a vast range of I_{Na} parameters (such as that used in OLS Figure 7), we

demonstrated that the AP is able to stably/steadily propagate for long time and over a long distance (up to 800 mm, well exceeding the size of rat or human heart) without firing an EAD. Only in the presence of an exacerbated structural substrate, an EAD would occur.

Another limitation results from the approximation of the curvature profile using (Eq. 4). Although the relationship between curvature and the location is clear in the distal region, that relationship might be questionable within the isthmus. As can be seen experimentally in the Figure 1B, a convex wavefront curvature can be seen inside the isthmus. That effect is however difficult to quantify and therefore we assumed a symmetric hyperbolic increase instead of simple zero curvature (planar wavefront). It is important to keep in mind that the curvature is never negative for the wavefront traveling from the isthmus into the expansion.

Reference List

Cabo, C., Pertsov, A. M., Baxter, W. T., Davidenko, J. M., Gray, R. A., & Jalife, J. (1994). Wave-front curvature as a cause of slow conduction and block in isolated cardiac muscle. *Circ.Res.* **75**, 1014-1028.

Faber, G. M. & Rudy, Y. (2000). Action potential and contractility changes in [Na(+)](i) overloaded cardiac myocytes: a simulation study. *Biophys.J.* **78**, 2392-2404.

Gray, R. A., Jalife, J., Panfilov, A., Baxter, W. T., Cabo, C., Davidenko, J. M., & Pertsov, A. M. (1995). Nonstationary vortexlike reentrant activity as a mechanism of polymorphic ventricular tachycardia in the isolated rabbit heart. *Circulation* **91**, 2454-2469.

Kucera, J. P., Kleber, A. G., & Rohr, S. (1998). Slow conduction in cardiac tissue, II: effects of branching tissue geometry. *Circ.Res.* **83**, 795-805.

Mironov, S. F., Vetter, F. J., & Pertsov, A. M. (2006). Fluorescence imaging of cardiac propagation: spectral properties and filtering of optical action potentials. *Am.J.Physiol Heart Circ.Physiol* **291**, H327-H335.

Munoz, V., Grzeda, K. R., Desplantez, T., Pandit, S. V., Mironov, S., Taffet, S. M., Rohr, S., Kleber, A. G., & Jalife, J. (2007). Adenoviral expression of IKs contributes to wavebreak and fibrillatory conduction in neonatal rat ventricular cardiomyocyte monolayers. *Circ.Res.* **101**, 475-483.

Rohr, S., Fluckiger-Labrada, R., & Kucera, J. P. (2003). Photolithographically defined deposition of attachment factors as a versatile method for patterning the growth of different cell types in culture. *Pflugers Arch.* **446**, 125-132.

Rohr, S., Kleber, A. G., & Kucera, J. P. (1999). Optical recording of impulse propagation in designer cultures. Cardiac tissue architectures inducing ultra-slow conduction. *Trends Cardiovasc.Med.* **9**, 173-179.

Rohr, S. & Kucera, J. P. (1997). Involvement of the calcium inward current in cardiac impulse propagation: induction of unidirectional conduction block by nifedipine and reversal by Bay K 8644. *Biophys.J.* **72**, 754-766.

Rohr, S. & Salzberg, B. M. (1994). Characterization of impulse propagation at the microscopic level across geometrically defined expansions of excitable tissue: multiple site optical recording of transmembrane voltage (MSORTV) in patterned growth heart cell cultures. *J.Gen.Physiol* **104**, 287-309.

Stocker, P. J. & Bennett, E. S. (2006). Differential sialylation modulates voltage-gated Na+ channel gating throughout the developing myocardium. *J.Gen.Physiol* **127**, 253-265.

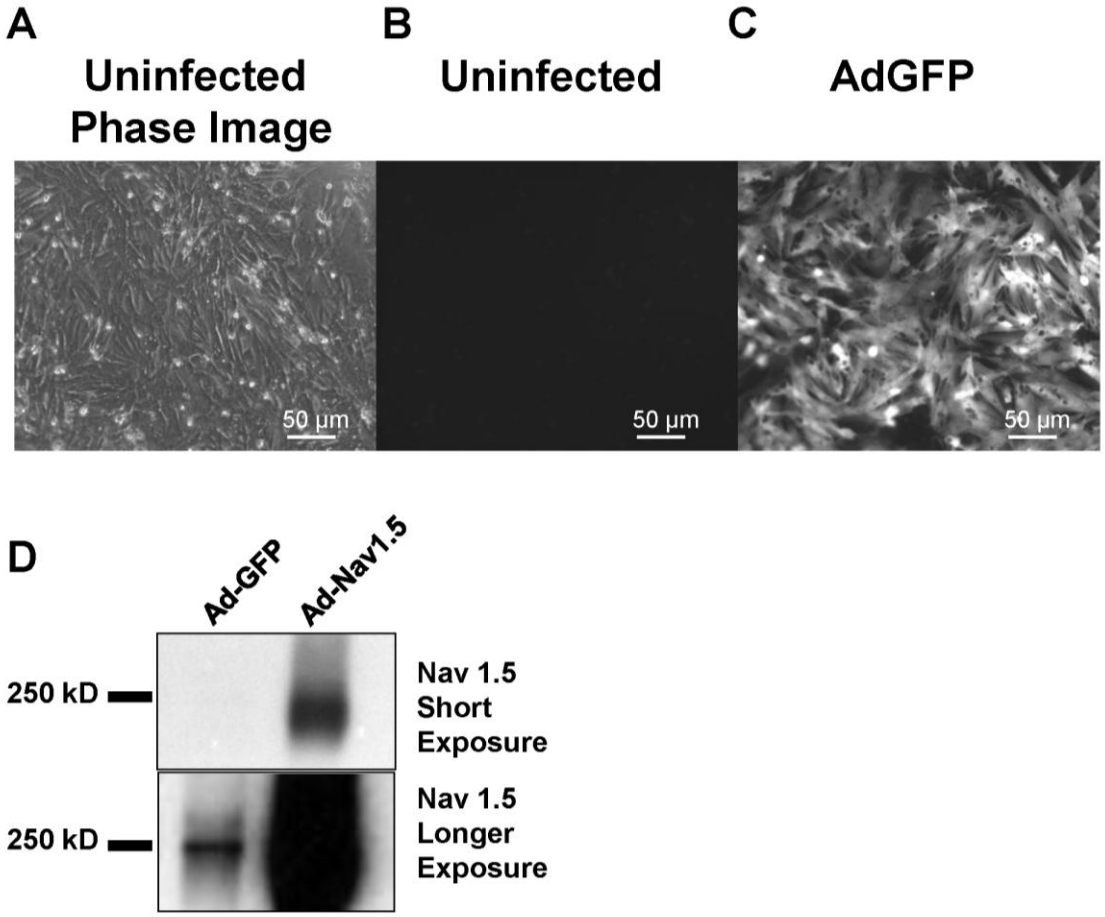

Figure 1: Adenoviral expression. A. Phase-contrast image of an uninfected monolayer. **(B & C)** Exposure time matched images of uninfected **(B, same field of view as A)** and Ad-GFP **(C)**. **D.** Representative Ad-Nav1.5 western blot demonstrating that despite the apparent absence of the Nav1.5 band in the Ad-GFP group **(Top)**, at a long exposure time **(Bottom)** the endogenous Nav1.5 band is apparent.

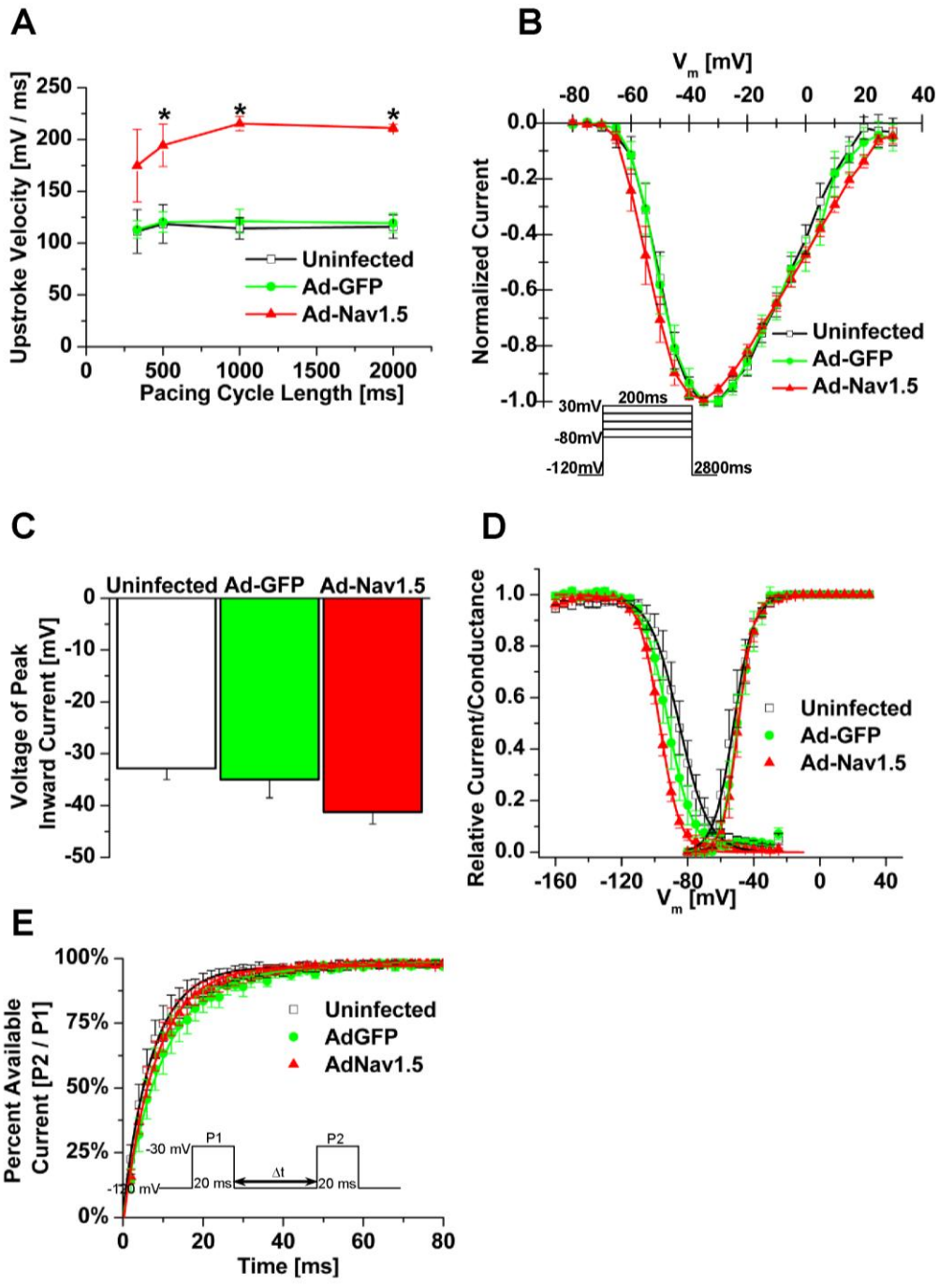

OLS Figure 2: Biophysical properties of I_{Na} in each group. A. Upstroke velocity for single cell current clamp APs (*=p<0.05 for Ad-Nav1.5 vs. Uninfected and Ad-GFP groups, N=2-4, n=3-6.) **B.** Normalized current-voltage relationship for Uninfected, Ad-GFP, and Ad-Nav1.5 NRVMs (N=6-8, n=8-12). **C.** Voltage of peak I_{Na} for each of the three groups. **D.** Voltage dependence of I_{Na} activation (N=6-8, n=8-12)and availability (N=3-4, n=5-7) of I_{Na} in Uninfected, Ad-GFP, and Ad-Nav1.5 NRVM groups. **E.** Time dependence of I_{Na} availability (P2/P1, N=5-6, n=6-10) Panels A-E: One-way ANOVA with Tukey Test.

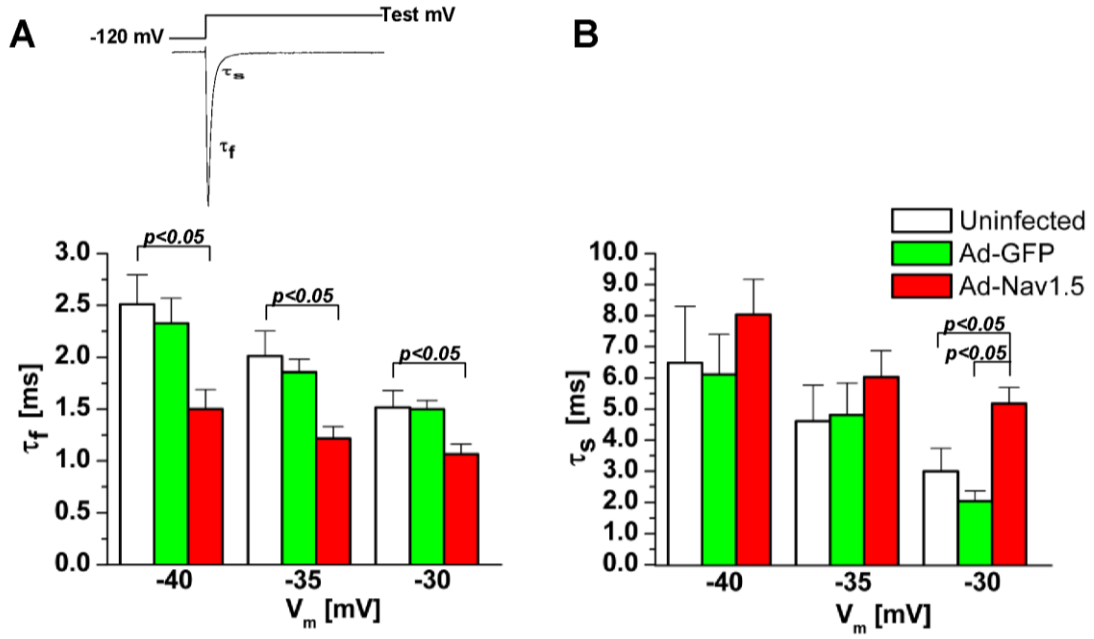

OLS Figure 3: I_{Na} Decay constants. A&B. I_{Na} fast and slow time constants of decay ($Tau_{f\&s}$, double exponential function,.N=6-8, n=7-12).

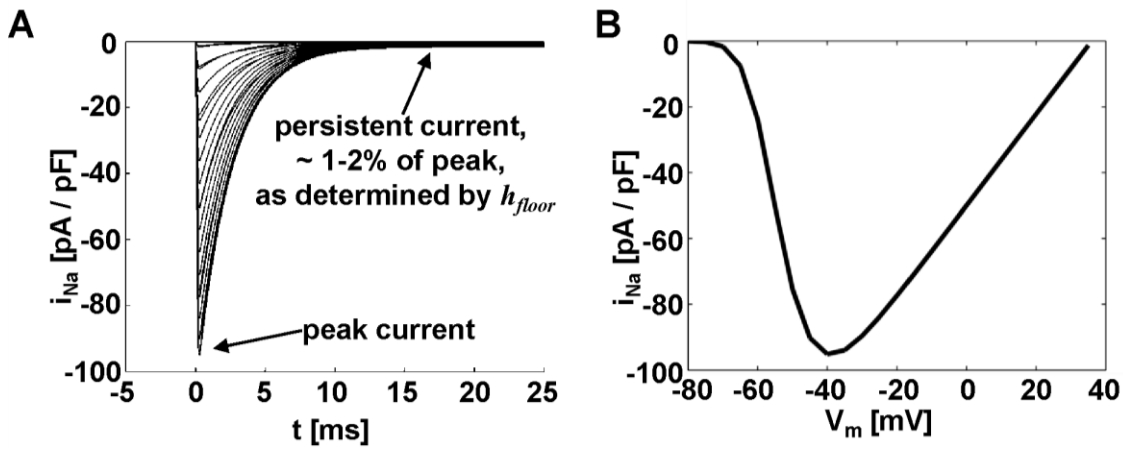

OLS Figure 4: Simulated voltage-clamp experiment. A. Family of current traces. **B.** I-V relationship..

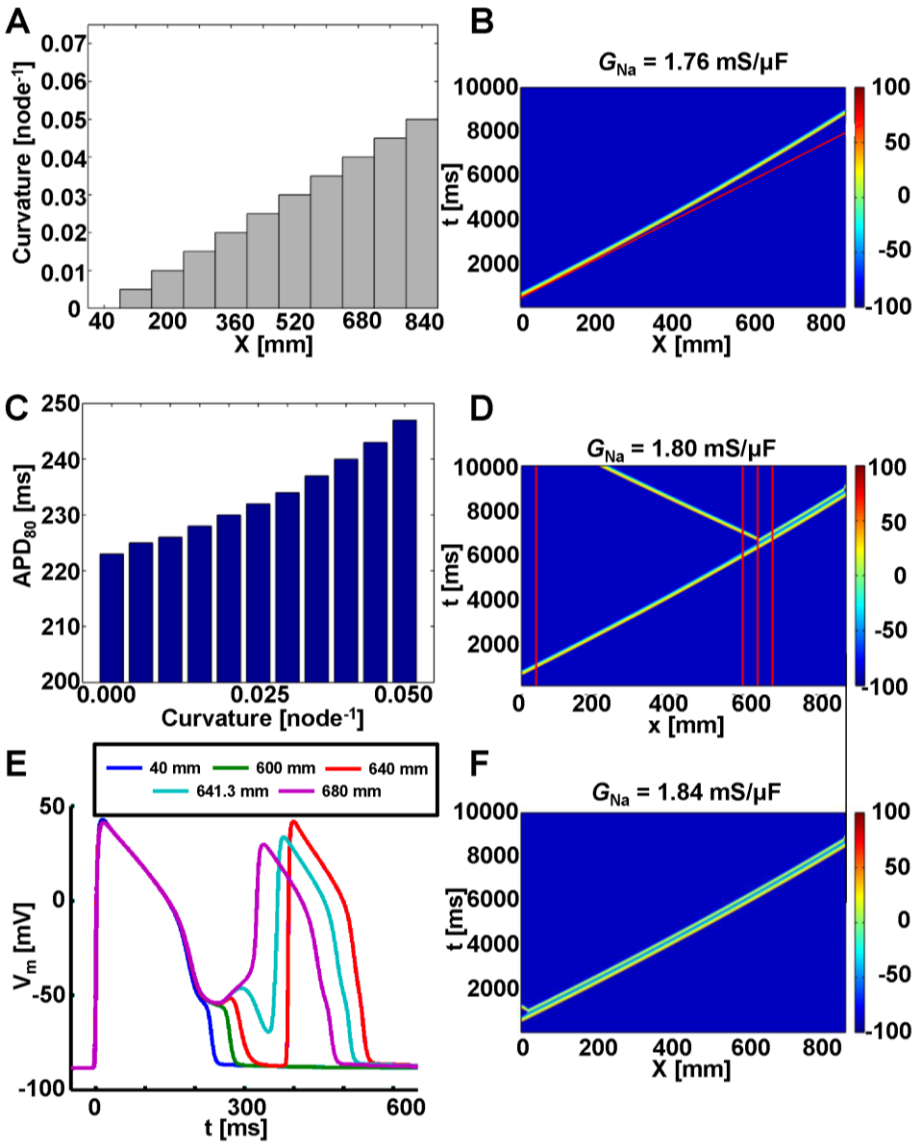

OLS Figure 5: Numerical Simulations of Reflection. A. Anatomy of a 1D cable with simulated curvature (see text for details). **B.** Time-space-plot showing a single propagated wave in the cable. Colorscale denotes transmembrane voltage (V_m) in millivolts. At low G_{Na}, the wave travels the entire cable undisturbed, even at the highest tested curvature, although CV decreases with increased curvature, as indicated by deviation from the straight red line, marking the initial CV. **C.** APDs at regions of increasing curvature, from the simulation shown in B. **D.** At a higher level of G_{Na}, at a specific curvature (0.04 node^{-1}, 0.4 mm^{-1}) an EAD occurs, which subsequently results in reflection, as well as a second antegrade propagated wave. Red vertical lines at 40, 600, 640, & 680mm denote the sites of AP and current traces in Panel E and OLS Figure 6 A-C, respectively. **E.** Time course of V_m at five distinct locations, marked by red vertical lines in **D**. All traces have been aligned so the upstroke of the APs preceding the reflected response occur at t=0. **F.** Additional increase in G_{Na} causes an EAD at a very small curvature (0.00 node^{-1}, 0.0 mm^{-1}), next to the stimulation site, and subsequently a double wave travels down the cable.

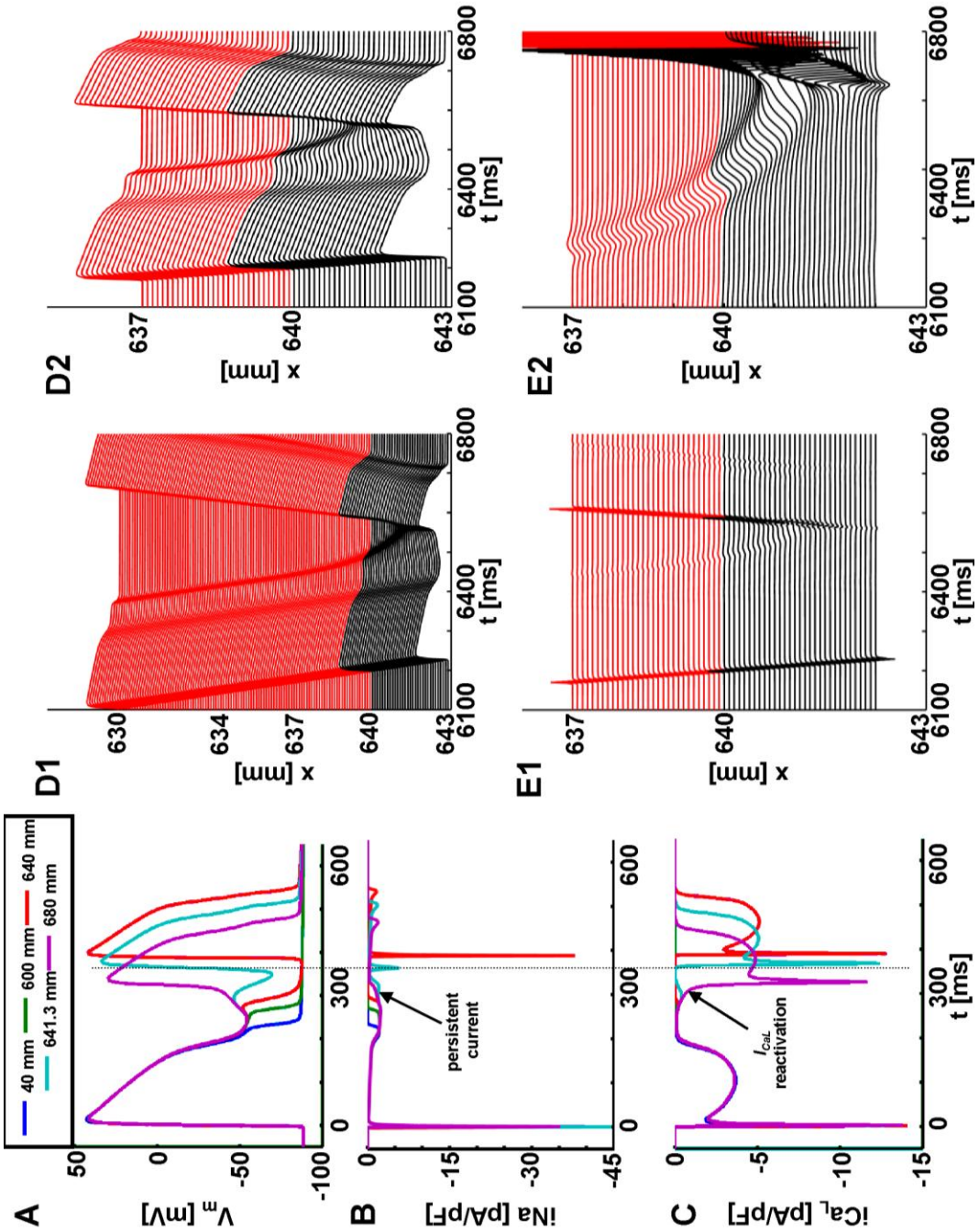

OLS Figure 6: Numerical Simulations of the Ionic and Electrotonic Currents Triggering Reflection. A-C. Time course of measurements observed at five distinct locations, marked with red vertical lines in **OLS Figure 5D.** All traces have been aligned so the upstroke occurs at *t*=0. **A.** Transmembrane voltage (V_m). **B.** Fast sodium current I_{Na}. **C.** L-type calcium current I_{CaL}. APs **D-E.** Red traces were recorded in the region upstream of 640 mm (curvature of 0.35 mm^{-1}) and black traces recorded at 640 mm and downstream (curvature of 0.40 mm^{-1}). **D1.** Action potentials recorded at the region of re-excitation (630-643mm). **D2.** Zoom-in view of panel **D1**. **E1.** Electrotonic current entering a cell at the region of re-excitation (637-643mm). **E2.** Zoom-in view of panel **E1**.

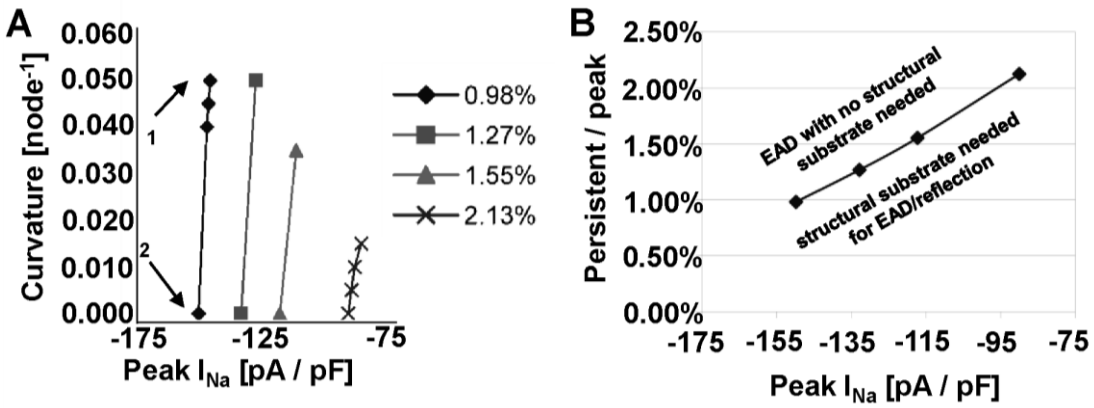

OLS Figure 7: Numerical simulations of the curvature and persistent/peak I_{Na} necessary for reflection. A. Curvature necessary for EAD/reflection as a function of G_{Na} and persistent I_{Na}. With persistent I_{Na} at 0.98% of peak I_{Na} and peak I_{Na} of -145.2 pA/pF, a cuvature as high as 0.05 node^{-1} (0.5 mm^{-1}) is needed to enable EAD/reflection (arrow 1). With peak I_{Na} of -149.7 pA/pF, EAD/reflection occur even at a planar wavefront (arrow 2). For higher percentages of persistent I_{Na}, this transition zone is shifted towards less negative peak I_{Na} (smaller amplitudes). **B.** Relationship between peak I_{Na} and persistent I_{Na} sufficient to cause EAD at a planar wavefront. Cells lying above/to the left of the line would not need any curvature to fire an EAD. Only the cells below/right of the line will experience curvature-dependent EADs.